Available online at www.sciencedirect.com
SCIENCE DIRECT®
Remote Sensing of Environment 90 (2004) 137–152
Remote Sensing of Environment
www.elsevier.com/locate/rse

Comparison of land surface emissivity and radiometric temperature derived from MODIS and ASTER sensors

Frédéric Jacob[a,b,*], François Petitcolin[c], Thomas Schmugge[a], Éric Vermote[d], Andrew French[e], Kenta Ogawa[a]

[a] USDA/ARS/Hydrology and Remote Sensing Laboratory, Building 007, BARC-West, Beltsville, MD 20705, USA
[b] Laboratoire de Télédétection et de Gestion des Territoires, Département Sciences et Méthodes, PURPAN-École supérieure d'agriculture, 75, voie du TOEC, 31076 Toulouse Cedex 3, France
[c] ACRI-ST, 260, route du Pin Montard, B.P. 234, 06904 Sophia Antipolis Cedex, France
[d] Department of Geography and NASA/GSFC, University of Maryland, Building 32, Room S36D, NASA/GSFC Code 923, Greenbelt, MD 20771, USA
[e] National Research Council Associateship, NASA/GSFC/Hydrological Sciences Branch, Code 974.1, Greenbelt, MD 20771, USA

Received 12 August 2003; received in revised form 24 November 2003; accepted 28 November 2003

Abstract

This study compared surface emissivity and radiometric temperature retrievals derived from data collected with the MODerate resolution Imaging Spectroradiometer (MODIS) and Advanced Spaceborne Thermal Emission Reflection Radiometer (ASTER) sensors, onboard the NASA's Earth Observation System (EOS)-TERRA satellite. Two study sites were selected: a semi-arid area located in northern Chihuahuan desert, USA, and a Savannah landscape located in central Africa. Atmospheric corrections were performed using the MODTRAN 4 atmospheric radiative transfer code along with atmospheric profiles generated by the National Center for Environmental Predictions (NCEP). Atmospheric radiative properties were derived from MODTRAN 4 calculations according to the sensor swaths, which yielded different strategies from one sensor to the other. The MODIS estimates were then computed using a designed Temperature-Independent Spectral Indices of Emissivity (TISIE) method. The ASTER estimates were derived using the Temperature Emissivity Separation (TES) algorithm. The MODIS and ASTER radiometric temperature retrievals were in good agreement when the atmospheric corrections were similar, with differences lower than 0.9 K. The emissivity estimates were compared for MODIS/ASTER matching bands at 8.5 and 11 μm. It was shown that the retrievals agreed well, with RMSD ranging from 0.005 to 0.015, and biases ranging from −0.01 to 0.005. At 8.5 μm, the ranges of emissivities from both sensors were very similar. At 11 μm, however, the ranges of MODIS values were broader than those of the ASTER estimates. The larger MODIS values were ascribed to the gray body problem of the TES algorithm, whereas the lower MODIS values were not consistent with field references. Finally, we assessed the combined effects of spatial variability and sensor resolution. It was shown that for the study areas we considered, these effects were not critical.

Keywords: MIR/TIR remote sensing; Surface emissivity and radiometric temperature; MODIS; ASTER; TISIE; TES; Atmospheric corrections; Spatial variability

1. Introduction

Knowledge of land surface temperature and broadband emissivity is of prime interest when studying energy and water balance of Earth, biosphere and atmosphere. Surface temperature is a key variable when dealing with exchanges between biosphere and atmosphere since it drives heat transfers at the surface–atmosphere interface (Jacob et al., 2002; Olioso et al., 1999, 2002; Schmugge & Kustas, 1999; Schmugge et al., 1998b). Surface broadband emissivity is a key variable when dealing with the Earth's radiation budget since it drives the surface longwave radiative balance (Ogawa et al., 2003; Zhou et al., 2003). Thermal InfraRed (TIR) remote sensing provides the unique possibility to retrieve surface temperature and broadband emissivity in a spatially distributed manner. Surface temperature can be derived from the channel radiances by estimating the channel emissivities (see the review by Dash et al.

* Corresponding author. Laboratoire de Télédétection et de Gestion des Territoires, Département Sciences et Méthodes, PURPAN-École Supérieure d'Agriculture, 75, voie du TOEC, 31076 Toulouse Cedex 3, France. Tel.: +33-56-115-2961; fax: +33-56-115-3060.
E-mail address: frederic.jacob@esa-purpan.fr (F. Jacob).

0034-4257/$ - see front matter © 2004 Elsevier Inc. All rights reserved.
doi:10.1016/j.rse.2003.11.015

(2002)). Surface broadband emissivity can be estimated as a linear combination of the channel estimates (Ogawa et al., 2002, 2003). Surface emissivity is defined as the ratio of the actual radiance emitted by a given surface to that emitted by a blackbody at the same thermodynamic (or kinetic) temperature. When dealing with remote sensing over heterogeneous land surfaces which display nonuniform distributions of temperature, the variables of interest are ensemble emissivity and radiometric temperature (Norman & Becker, 1995). Radiometric temperature is then equal to kinetic temperature for a homogeneous and isothermal surface (Becker & Li, 1995). However, surface heterogeneities induce nonlinear effects that can affect the validity of the assumptions made to retrieve emissivity and radiometric temperature. This may be a critical issue since natural landscapes can display significant spatial variability of emissivity (Ogawa et al., 2002).

Among the several sensors on board the NASA's Earth Observation System (EOS) TERRA (formerly EOS-AM1) platform that was launched in 1999, the Advanced Spaceborne Thermal Emission Reflection Radiometer (ASTER) and MODerate resolution Imaging Spectroradiometer (MODIS) instruments were designed to provide high quality observations of land surfaces, atmosphere and oceans. ASTER was designed to collect data over shortwave and longwave infrared domains for geological applications (Yamaguchi et al., 1998). Therefore, its spectral features were set to provide a good sampling of the TIR emissivity spectral variations. Another important objective was acquiring high spatial resolution data to study upscaling processes which occur when considering coarser resolutions, i.e. nonlinear effects induced by the use of models designed for homogeneous surfaces over heterogeneous pixels. MODIS was designed to collect, at a moderate spatial resolution (i.e. kilometer resolution), multiangular observations over a wide spectral range, with almost daily coverage of the Earth (Justice et al., 1998). Therefore, the sensor provides multitemporal and multidirectional remotely sensed data within several spectral bands over the Middle InfraRed (MIR) and TIR domains.

Several algorithms have been developed these two last decades to accurately estimate surface emissivity and radiometric temperature, with the goal to reach an accuracy ranging between 0.8 and 1 K for surface temperature (Seguin et al., 1999). These algorithms rely on methods which use the available information according to the spectral, directional and temporal features of the considered sensors. Two widely accepted approaches are the Temperature Emissivity Separation (TES) algorithm (Gillespie et al., 1996, 1998; Schmugge et al., 1998a, 2002a) and the Temperature-Independent Spectral Indices of Emissivity (TISIE) approach (Becker & Li, 1990; Li & Becker, 1993; Nerry et al., 1998; Petitcolin et al., 2002a,b; Petitcolin & Vermote, 2002). TES was developed for the spectral features of ASTER which yield single temporal and mono directional observations within several spectral bands over the TIR domain. TISIE was developed to use the information provided by multidirectional and multitemporal MIR/TIR data, such as those collected by MODIS. The performances of the TES algorithm were theoretically and experimentally assessed by Gillespie et al. (1996, 1998), and Schmugge et al. (1998a, 2002a). The performances of the TISIE algorithm were analyzed by Nerry et al. (1998), Petitcolin et al. (2002a,b), and Petitcolin and Vermote (2002). The results reported by these studies yielded accuracies around 0.01 and 1 K for surface emissivity and radiometric temperature, respectively.

In this study, we proposed to compare ASTER and MODIS emissivity/radiometric temperature estimates derived from the TES and TISIE algorithms designed by Schmugge et al. (1998a) and Petitcolin and Vermote (2002), respectively. Performing such a comparison was of interest for several reasons. First, the considered algorithms relied on different assumptions according to the temporal, directional and spectral information provided by each sensor. Consequently, considering numerous environmental situations depicted by MODIS/ASTER scenes, a comparison of the TES and TISIE retrievals allowed assessing the consistency between the algorithms. ASTER and MODIS are on the same platform, which provides the opportunity to perform such a comparison for the first time. Indeed, acquisition time is critical for TIR observations because of the nonstable nature of the kinetic temperature. Therefore, comparing algorithm retrievals was unique and provided complementary investigations to validation studies which require much effort to account for numerous environmental situations. Once the consistency between the algorithms was shown, the second interest of this comparison was the possibility to assess problems related to upscaling issues such as nonlinear effects induced by spatial heterogeneity. Since algorithms devoted to the retrieval of surface radiometric temperature and emissivity are generally based on nonlinear equation systems, their application over heterogeneous areas introduces a dependence on spatial resolution. Indeed, averaging algorithm outputs or running algorithms on averaged inputs may provide results which significantly differ. This is a critical issue for further investigations based on knowledge of surface radiometric temperature and emissivity, such as estimating Earth's radiation budget or energetic exchanges at the surface–atmosphere interface using kilometric resolution sensors.

In this paper, we considered two sets of MODIS/ASTER scenes collected over two areas. The first area was located in the Central African Republic; and the second area was located in northern Chihuahuan desert, New Mexico, USA. This yields a data set which included numerous land use situations: Savannah landscape, semi-arid rangelands, mountainous areas, irrigated agricultural areas and gypsum sand dunes. Atmospheric corrections were performed using the MODTRAN 4 radiative transfer model (Berk et al., 1998) along with atmospheric profiles provided by the National Center for Environmental Prediction (NCEP). In

order to minimize the discrepancies between MODIS/TISIE and ASTER/TES retrievals due to factors other than the algorithm differences, we used the same atmospheric profiles for both sensors when characterizing atmosphere state for MODTRAN 4 calculations. Next, ASTER and MODIS surface emissivity/radiometric temperature were computed using the TES and TISIE algorithms, respectively. For a better understanding of possible differences between the MODIS and ASTER retrievals because of the experimental context (sensor instrumental features, magnitude of the atmospheric corrections, land use occupation), we first compared intermediate variables such as brightness temperature at the sensor and ground levels. Brightness temperatures and emissivities were compared for the ASTER/MODIS matching bands at 8.6 and 11 μm (see Fig. 1). Finally, we assessed the combined effects of spatial variability and sensor resolution. This was performed intercomparing ASTER and MODIS retrievals of surface radiometric temperature for different levels of spatial variability of the ASTER aggregated values inside MODIS pixels. After the description of the sensors and the corresponding algorithms, we describe the data preprocessing, and next report the comparison results.

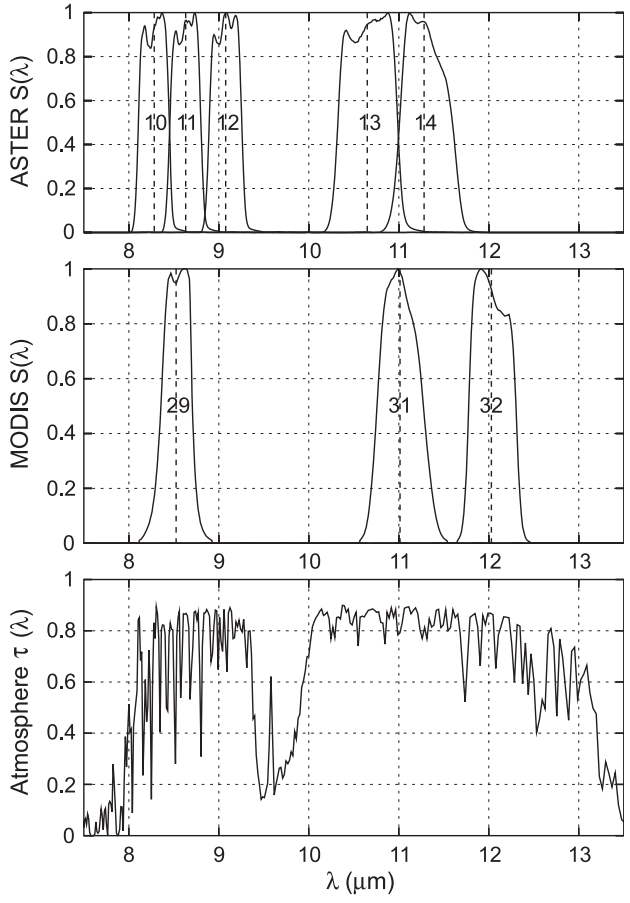

Fig. 1. Illustration of the sensor spectral response functions (solid lines) and the corresponding channel averaged wavelengths (dashed lines), over the TIR domain for both ASTER (first subplot, channels numbered 10 to 14) and MODIS (second subplot, channels numbered 29 to 32). The example of atmospheric transmittance spectrum (third subplot) was simulated using MODTRAN 4 along with one of the atmospheric profiles used in this study (see Section 2.3.2), when considering a nadir view angle.

2. Material and methods

2.1. The sensors

Both ASTER and MODIS are on EOS-TERRA, a sun-synchronous platform with a 10:30 am descending equator crossing. The ASTER TIR sensor is a five-band nadir viewing scanner ($\pm 3°$), pointable to $\pm 8.5°$, with a 90 m spatial resolution and a 63 km swath. As a consequence of its high spatial resolution, the sensor has a temporal repetitivity of 16 days. The MODIS sensor is an across track scanner ($\pm 55°$) that collects, amongst other data, radiance measurements in six bands designed for land surface temperature applications over the MIR (3–5 μm) and TIR (8–12 μm) spectral ranges. The nadir spatial resolution is 1 km, and the nominal swath is 2330 km. As a consequence of its wide swath capability, the sensor provides almost global coverage twice a day (ascending and descending orbits), with a revisit in the same observation configuration every 16 days. Therefore, the collected data sets provide directional samplings of the considered signals within this temporal window. Since they are carried by the same spacecraft, MODIS and ASTER collect coincident nadir observations. Fig. 1 displays the channel filter response functions over the TIR domain for both sensors, and a typical example of atmospheric transmittance spectra calculated using the MODTRAN 4 radiative transfer code along with the atmospheric profiles we considered in this study (see Section 2.3.2). The five ASTER TIR bands (numbered 10 to 14) are centered around 8.28, 8.63, 9.07, 10.65 and 11.28 μm. For MODIS, the three MIR bands (20, 22 and 23) are centered around 3.75, 3.95 and 4.05 μm, and the three TIR channels (29, 31 and 32) are centered around 8.55, 11.03 and 12.02 μm. Fig. 1 shows that MODIS band 29 matches ASTER band 11. MODIS band 31 overlaps both ASTER bands 13 and 14. Since spectral variations of emissivity are generally small around 11 μm, we could compare either bands 31/13 or bands 31/14. Indeed, we observed that the two comparison schemes gave very similar results. From the channel filter response functions and the atmospheric transmittance spectra calculated using MODTRAN 4, we computed the waveband averaged atmospheric transmittance over the ASTER and MODIS channels. A typical example (Table 1) shows that MODIS channels 29 and 31 have slightly lower transmittances ($\sim$ 1–2%) than do ASTER channels 11 and 13. The situation is reversed for the longer wavelengths, where ASTER channel 14 has $\sim$ 1% lower transmittance than MODIS channel 31. Since ASTER has no MIR band and MODIS has three TIR bands only, the MODIS MIR channels 20, 22, 23 and the ASTER TIR channels 10 and 12 were not considered when comparing

Table 1
Numerical values of waveband averaged atmospheric transmittance τ_a over ASTER (top) and MODIS (bottom) channels, when considering the atmospheric transmittance spectra displayed in Fig. 1

ASTER						
Bands	10	11	12	13	14	
τ_a	0.6697	0.7560	0.8144	0.8462	0.8252	
MODIS						
Bands	29	31	32			
τ_a	0.7398	0.8353	0.7827			

The gray cells correspond to the intercompared ASTER/MODIS channels, i.e. 11/29, 13/31 and 14/31.

brightness temperatures at the sensor and ground levels, and surface emissivity retrievals.

2.2. The MODIS/TISIE and ASTER/TES algorithms

Accurate estimation of surface emissivity and radiometric temperature from TIR remote sensing is a difficult task that requires separating their combined effects on the measured radiance. Indeed, separating surface emissivities and radiometric temperature is an under-determined problem since there is one more unknown than measurements. Consequently, over the past two decades much effort has been made to develop useful separation methods, as detailed by the reviews of Barducci and Pippi (1996); Caselles et al. (1997); Dash et al. (2002); Li et al. (1999) and Sobrino et al. (2000). There are essentially four types of separation methods: (1) split-window, (2) day–night pair, (3) Temperature-Independent Spectral Indices (TISIE), and (4) TIR spectral contrast. The split-window method, focused on land surface temperature, gave birth to many algorithms, some of them using auxiliary information derived from either vegetation indices (Sobrino & Raissouni, 2000; Valor & Caselles, 1996) or land surface type classification (Snyder et al., 1998; Wan & Dozier, 1996). The day–night pair method proposed by Wan and Li (1997) for the MODIS data relies on the iterative inversion of a simplified direct modeling of measurements. The system is then conditioned by the use of daytime and night-time consecutive observations, inducing equal numbers of equations and unknowns. The TISIE method, originally developed by Becker and Li (1990) will be detailed further when presenting the MODIS/TISIE algorithm (Section 2.2.1). The last family of algorithms is based on the use of the spectral variation of emissivity over the TIR domain (Barducci and Pippi, 1996; Coll et al., 2000; Gillespie et al., 1998), among which the TES method was designed by Gillespie et al. (1996, 1998) for the ASTER instrument. As explained in Introduction, TES and TISIE were based on different assumptions which relied on the use of different types of remote sensing information. The TES algorithm relied on an empirical relation between the range of observed TIR emissivities and their minimum value. Therefore, it required multispectral information over the TIR domain, but did not need either multidirectional or multitemporal observations. The TISIE algorithm relied on MIR/TIR emissivity ratios raised to specific powers, along with a good estimation of the MIR emissivity by characterizing well the corresponding Bidirectional Reflectance Distribution Function (BRDF). Therefore, it required remotely sensed data over the MIR and TIR spectral ranges, daytime and nighttime consecutive observations, as well as multidirectional observations within a 16-day period which corresponded to the angular sampling of the required signals. The algorithms we considered in this study were the TISIE version developed by Petitcolin and Vermote (2002) for MODIS, and the TES version proposed by Schmugge et al. (1998a, 2002a). Below are overviews of the algorithms. Detailed descriptions of the MODIS/TISIE algorithm are given by Petitcolin et al. (2002a,b), and Petitcolin and Vermote (2002). Detailed descriptions of the ASTER/TES algorithm can be found in Gillespie et al. (1996, 1998) and Schmugge et al. (1998a, 2002a).

2.2.1. The MODIS/TISIE algorithm

The basic idea of the TISIE approach, originally proposed by Becker and Li (1990), consists of calculating ratios of emissivities raised to specific power to characterize the emissivity relative variations without influence of surface temperature. This is performed by both (1) using the Slater's approximation which expresses the surface emitted radiance L_k over a channel k as a power function of the radiometric temperature T: $L_k = a_k T^n{}_k$; and (2) expressing the surface outgoing radiance as $L_{gk} = \varepsilon_k L_k C_k$ where ε_k is the channel emissivity, and C_k a corrective factor which accounts for the surface reflection of the atmospheric downwelling radiance (Nerry et al., 1998). Then, the index TISIE_{ji} characterizes the emissivity relative variation between two channels i and j:

$$\mathrm{TISIE}_{ji} = \frac{\varepsilon_j}{\varepsilon_i^{n_j/n_i}} = \varepsilon_j(\varepsilon_i)^{-n_{ji}} = \frac{a_i^{n_{ji}}}{a_j}\frac{L_{gj}}{C_j}\left[\frac{C_i}{L_{gi}}\right]^{n_{ji}} \quad (1)$$

Li and Becker (1993) and Nerry et al. (1998) proposed next to use consecutive nighttime and daytime observations over the MIR and TIR channels j and i, to derive the magnitude of the MIR emissivity ε_j from the corresponding bidirectional reflectance ρ_j by using the Kirchhoff's law $\varepsilon_j = 1 - \rho_j$. The MIR bidirectional reflectance ρ_j is retrieved from the daytime MIR and TIR observations:

$$\begin{aligned}\rho_j &= \frac{1}{E_j^{\mathrm{sun}}}[L_{gj}^{\mathrm{day}} - L_e] \\ &= \frac{1}{E_j^{\mathrm{sun}}}\left[L_{gj}^{\mathrm{day}} - TISIE_{ji}\frac{a_j}{a_i n_{ji}}\frac{C_j^{\mathrm{day}}}{[C_i^{\mathrm{day}}]^{n_{ji}}}[L_{gi}^{\mathrm{day}}]^{n_{ji}}\right]\end{aligned} \quad (2)$$

where E_j^{sun} is the incoming solar spectral radiance. The MIR emission component L_e is calculated using both the daytime surface outgoing radiance L_{gi}^{day} over the TIR channel i, and daytime TISIE_{ji}. The latter is assumed to

be equal to the nighttime $TISIE_{ji}$, derived from the corresponding observations along with Eq. (1).

When a multidirectional data set of MIR bidirectional reflectance ρ_j can be derived from multiangular MIR/TIR measurements along with Eq. (2), it is possible to characterize the MIR BRDF and next compute the MIR hemispherical–directional reflectance using an integration over illumination angles. The MIR directional emissivity can then be derived from the MIR hemispherical–directional reflectance using the Kirchhoff's law. Petitcolin et al. (2002a,b) used the Advanced Very High Resolution Radiometer (AVHRR) multiangular information to invert a simple BRDF parameterization model. Petitcolin and Vermote (2002) proposed next an improvement by using the MODIS multidirectional capabilities along with a BRDF kernel-driven model such as Li-Sparse/Ross Thick (Wanner et al., 1995). A flowchart of the algorithm is given in Fig. 2. In order to reduce the instrumental noise occurring over the MIR spectral range when characterizing the BRDF from Eq. (2), $TISIE_{ji}$ are calculated as averaged values over the 16-day period centered around acquisition dates of nadir observations. Finally, daytime TIR emissivity ε_i is derived from MIR emissivity ε_j using Eq. (1), which allows retrieving radiometric temperature. Considering averaged values of TISIE over a 16-day period and

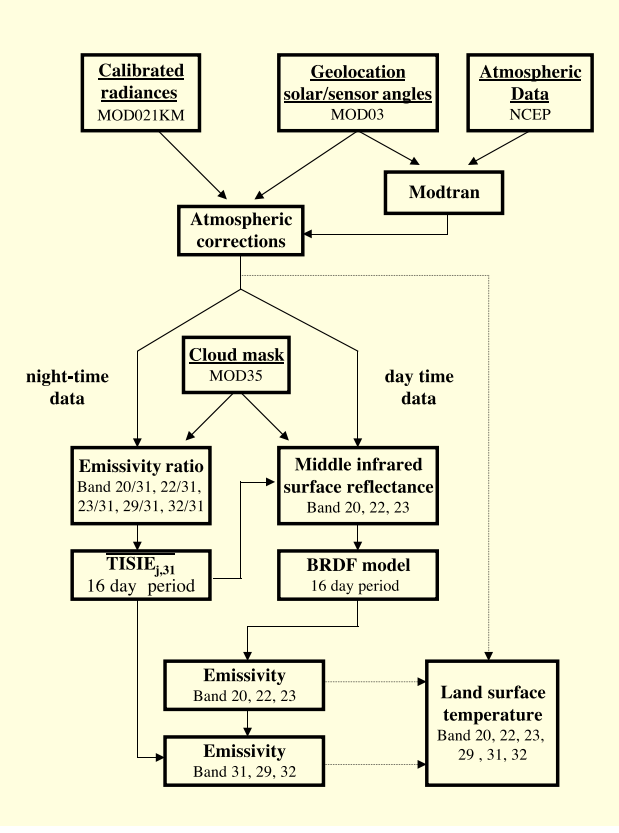

Fig. 2. Flowchart of the TISIE algorithm used to derived MIR and TIR emissivities when considering anyone of the MODIS MIR channels (20, 22 or 23) and the MODIS TIR channel 31 to compute the TISIE (from Petitcolin & Vermote, 2002).

inverting a kernel-driven BRDF model over a multidirectional data set collected during the same period relied on the assumption that changes in land surface status within this temporal window do not impact dramatically either TISIE or MIR BRDF. This was analyzed and discussed in details by Nerry et al. (1998), Petitcolin et al. (2002a,b), and Petitcolin and Vermote (2002). We note that the algorithm could use any of the three MODIS MIR and TIR channels since Petitcolin and Vermote (2002) showed the consistency between the retrievals regardless of chosen channels.

2.2.2. The ASTER/TES algorithm

The TES algorithm combines interesting features of three previous approaches, with improvements to obtain a better accuracy on the estimates of emissivity absolute values. It is closely related to the Mean-MMD method proposed by Matsunaga (1994), and uses the Normalized Emissivity Method (NEM, (Gillespie, 1985)) to estimate surface radiometric temperature, from which emissivity ratios are derived using the Ratio algorithm (Watson, 1992). In order to reduce instrumental noise, the spectral shape of emissivity is derived using ratios of channel emissivities to their mean value $\bar{\varepsilon}$. The magnitude is estimated using a relationship between the emissivity minimum value $\varepsilon_{\min}$ and the amplitude of emissivity spectral variations. The latter is characterized using the Maximum Minimum Difference (MMD), i.e. the ratio of the difference between the emissivity maximum and minimum values (i.e. $\varepsilon_{\max}$ and $\varepsilon_{\min}$) to the mean value $\bar{\varepsilon}$:

$$\mathrm{MMD} = \frac{\varepsilon_{\max} - \varepsilon_{\min}}{\bar{\varepsilon}} \tag{3}$$

Therefore, the algorithm relies on a semi-empirical power-law relationship between $\varepsilon_{\min}$ and MMD, such as $\varepsilon_{\min}$ decreases when MMD increases (see Fig. 1 in Schmugge et al. (1998a)):

$$\varepsilon_{\min} = A + B \times \mathrm{MMD}^C \tag{4}$$

This relationship requires a previous calibration of the A, B, C coefficients over a database of measured emissivity spectra. In this study, we used coefficients proposed by Schmugge et al. (1998a) and calibrated over samples collected around the world: $A = 0.994$, $B = -0.687$, $C = 0.737$. Calculation of MMD requires knowledge of minimum, maximum and mean values of emissivity. The latter are deduced from surface emitted radiances by estimating the actual radiometric temperature as the maximum of the estimated radiometric temperatures for the channels of the considered sensor. Since TES consists of solving a nonlinear equation system, it requires a three-iteration convergent process, along with initial guesses of channel emissivities. The latter are computed in an optimized way based on the NEM approach.

The TES algorithm was theoretically and experimentally analyzed by Gillespie et al. (1996, 1998), and Schmugge et al. (1998a). Next, it was successfully applied by Schmugge et al. (2002a) on the HAPEX-Sahel/Thermal Infrared Mul-

tispectral Scanner (TIMS) data set, and by Schmugge et al. (2002b) on ASTER data collected over the Jornada Range located in northern Chihuahuan desert, New Mexico, USA. In the present study, the TES algorithm was applied to single directional ASTER data collected at a given time. Therefore, the ASTER emissivities were instantaneous estimates, as compared to the MODIS emissivities derived from measurements collected over 16-day periods.

2.3. Data set: description and preprocessing

2.3.1. The Jornada and central African republic data sets

The two areas selected for the comparison were located in the Central African Republic and in southern New Mexico, USA. The Africa scenes were collected over the St-Floris National Park (latitude 9.54°N, longitude 21.53°E). They were chosen for the validation of a new fire detection algorithm (Petitcolin & Vermote, 2002) since the scenes included many active fires. The area was typical of a Savannah landscape during the fall burning season, and displayed a patch of heterogeneous patterns. The USA scenes covered the United State Department of Agriculture/Agricultural Research Service/Jornada Experimental Range (USDA/ARS/JER, latitude 32.57°N, longitude 106.58°W). This area is a Long-Term Ecological Research (LTER) site where the USDA/ARS conducts the JORNada EXperiment (JORNEX), which consists of collecting semi-annual remotely sensed data from ground, airborne and satellite platforms (Havstad et al., 2000). The study site, located in the northern Chihuahuan desert, is typical of a semi-arid region with sparse vegetation including grass, mesquite, tarbush and creosote bushes. The ASTER scene represented a heterogeneous pattern since it included the San Andres mountain chain, semi-arid rangelands, the irrigated agricultural areas along the Rio Grande, and the White Sands National Monument, an area of extensive gypsum sand dunes. The ASTER/MODIS scenes, corresponding to coincident nadir observations, were acquired on November 23, 2000 over Africa and May 12, 2001 over the Jornada, around 10:30 am at local solar time, i.e. 10:25 am Standard Time for Africa and 11:00 am Mountain Standard Time for the Jornada. The preprocessed images were provided on-line by the United States Geological Survey/Distributed Active Archive Center/Earth Resources Observation System (EROS) Data Center (USGS/DAAC/EDC), and consisted of radiometrically and geometrically corrected radiances at the sensor level. The scene sizes approximately corresponded to the sensor swath dimensions, i.e. squares of 63×63 and 2330×2330 km^2, for ASTER and MODIS, respectively. These images of brightness temperature at the sensor level were provided with estimated accuracies about 0.1 K for MODIS (Xiong et al., 2002) and 1 K for ASTER (Fujisada, 1998; Fujisada et al., 1998). We observed brightness temperature values ranging between 295 and 320 K for both the Africa and Jornada scenes, indicating that the observed targets were hot surfaces. However, the mean value was higher for the Jornada (around 315 K) than for Africa (around 305 K).

2.3.2. Atmospheric corrections

Both the TES and TISIE algorithms required band by band atmospheric corrections, to obtain estimates of surface outgoing and atmospheric downwelling radiances. These were performed using the radiative transfer model MODTRAN 4 along with atmospheric profiles generated by the National Center for Environmental Prediction (NCEP). As explained in Introduction, we used the same atmospheric profiles for both sensors when characterizing atmosphere state for MODTRAN 4 calculations. The latter were then used to compute MODIS and ASTER waveband integrated values of the atmospheric radiative properties: transmittance τ_{atm}, upwelling and downwelling radiance $L_{atm}^{\uparrow}$ and $L_{atm}^{\downarrow}$. Surface outgoing radiance L_{sur} was next derived from at sensor radiance L_{sen} using the radiative transfer equation:

$$L_{sur} = \frac{L_{sen} - L_{atm}^{\uparrow}}{\tau_{atm}} \quad (5)$$

The NCEP profiles were generated using a reanalysis procedure which incorporated the relevant measurements in an atmospheric model to produce a consistent representation of the atmosphere (Derber et al., 1991; Derber & Wu, 1998). They provided estimates of pressure, temperature and humidity from 1000 to 10 mb, and were available on a grid having a spatial resolution of 1° in latitude/longitude.

The choice of atmospheric correction strategies was driven by the swath dimensions of the sensors. Since that of ASTER was about 63 km, i.e. around 0.5° in latitude/longitude, the closest NCEP profile was used, and we therefore assumed that the atmospheric radiative properties

Table 2
Values of atmospheric Water Vapor Content (WVC) estimated from the four NCEP profiles used to process the MODIS data and surrounding the ASTER scenes

Sensor and scene	Profile	WVC (g cm^{-2})
MODIS Africa	Raw NCEP (N 09°, E 021°)	1.63
	Raw NCEP (N 09°, E 022°)	1.70
	Raw NCEP (N 10°, E 021°)	1.54
	Raw NCEP (N 10°, E 022°)	1.58
	Mean value	1.61
	Max – Min	0.16
ASTER Africa	Raw NCEP (N 10°, E 022°)	1.58
MODIS Jornada	Raw NCEP (N 32°, W 106°)	2.19
	Raw NCEP (N 32°, W 107°)	1.92
	Raw NCEP (N 33°, W 106°)	2.06
	Raw NCEP (N 33°, W 107°)	1.77
	Mean value	1.98
	Max – Min	0.41
ASTER Jornada	Raw NCEP (N 33°, W 107°)	1.77
	Adjusted NCEP	1.89

The profile the closest to the ASTER scene amongst these four was used to atmospherically correct the ASTER data. Numbers between parenthesis correspond to the latitude and longitude of the profiles.

were uniform within the scene. For the MODIS data, however, the 2330 km swath dimension required accounting for the spatial variability of these radiative properties within the scene. For this, we used a spatial interpolation procedure. The MODTRAN 4 calculations were performed for each profile of the NCEP grid included within the MODIS scene. Then, the atmospheric radiative variables computed from MODTRAN 4 calculations (i.e. transmittance, upwelling and downwelling radiances) were bilinearly interpolated to each MODIS pixel. The validity of this spatial interpolation procedure was previously verified by Petitcolin and Vermote (2002). The NCEP profiles, which started at 1000 mb pressure level, were truncated according to the ground altitude at the profile locations. Moreover, ground-based meteorological measurements were routinely collected at the Jornada Range. Therefore, in addition to the NCEP profile used to process the ASTER data collected over the Jornada, we also considered an adjusted profile incorporating surface temperature and humidity conditions recorded on site. By using such an adjusted profile, it was assumed to provide more realistic information when characterizing the atmosphere, as compared to the NCEP profile, although the spatial variation of surface temperature and humidity conditions could be significant within the 63×63 km^2 size ASTER scene. This adjusted profile was not considered when performing atmospheric corrections on MODIS data since

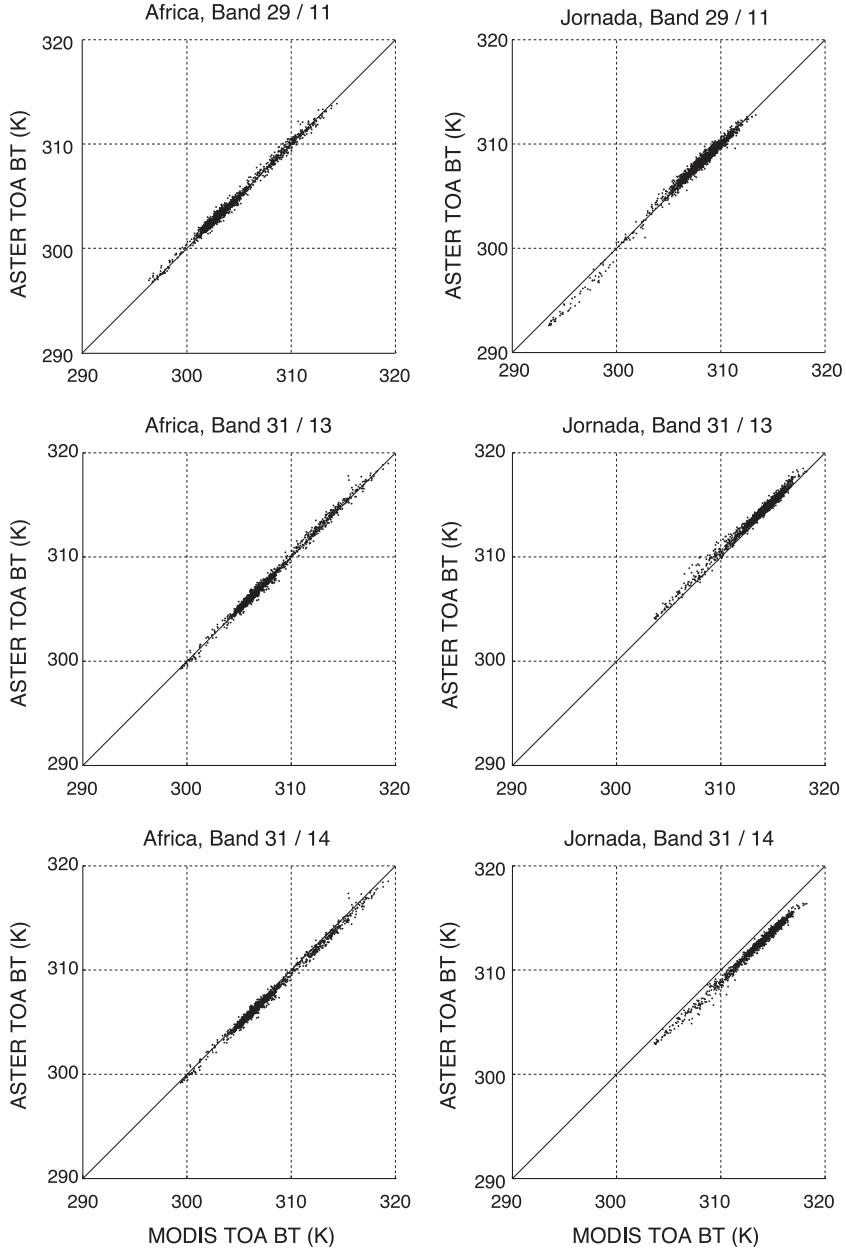

Fig. 3. Scatterplots of MODIS and ASTER Top of Atmosphere (TOA) Brightness Temperatures (BT) for both the Africa and Jornada scenes. The solid line is the 1:1 line.

the procedure we used for this sensor was based on a spatial interpolation. We note that the atmospheric corrections of the MODIS data were performed for the daytime and nighttime observations collected within the 16-day temporal window.

As mentioned previously (Section 2.3.1), we noted large values of brightness temperature at the sensor level, which corresponded to large values of surface temperature. According to the observations reported by Jacob et al. (2003), the dominant atmospheric effect when observing hot surfaces is absorption by atmospheric water vapor. The latter drives the atmospheric transmittance (Becker, 1987) such as an increase of water vapor induces a decrease of atmospheric transmittance. Consequently, using a wetter atmospheric profile induces larger surface brightness temperatures after atmospheric corrections (see Eq. (5)). Since we used different atmospheric correction strategies according to the sensor swaths, we first compared the atmospheric Water Vapor Content (WVC) of the four profiles surrounding the ASTER scene (see Table 2). Both the magnitude and the variability of these WVC values were lower for Africa as compared to the Jornada. For Africa, the profile closest to the ASTER scene had a WVC slightly lower than the mean value over the four surrounding profiles. For the Jornada, we observed the same trend, but the difference was larger. The adjusted profile used to process the ASTER scene collected over the Jornada had an intermediate WVC value between that of the closest profile and the mean value over the four surrounding profiles. These observations will be further used to explain the differences between the ASTER and MODIS brightness temperatures at the sensor and ground levels.

2.3.3. Superposition of the MODIS and ASTER images

The last step of the preprocessing dealt with the superposition of the MODIS and ASTER coincident nadir images, which consisted of aggregating the ASTER pixels matching the footprint of each MODIS pixel. The georegistration information was provided together with the radiance data. Those we considered to perform the superposition were (1) the geographic location of the center of each MODIS pixel, (2) the geographic coordinates of the center of the ASTER scene, and (3) the rotation angle between the ASTER radiance images and the Universal Transverse Mercator (UTM) projection to be used. Since both instruments were on the same platform, the accuracy of the image superposition was expected to be very good, although it could not be assessed. As a consequence of the triangular line spread function of the MODIS sensor (Barnes et al., 1998), the MODIS pixel footprint was about 1 km along track and 2 km across track. Therefore, we applied to each ASTER pixel a triangular-symmetric weighting function that accounted for the across track distance between the considered pixel and the center of the corresponding MODIS pixel.

In order to assess the impact of surface heterogeneities within MODIS pixels, we performed the comparisons of MODIS and ASTER surface radiometric temperature retrievals by considering different levels of variability of the 11×11 aggregated ASTER values (90 m) inside the corresponding MODIS pixel (1 km). If the standard deviation of the radiometric temperature was larger than a given threshold value, the MODIS and ASTER pixels were not considered. The threshold values we choose were 2.5, 1 and 0.5 K, respectively. In the following, we first present the comparison results we obtained when considering the 2.5 K threshold value. We note that we obtained very similar comparison results when considering either the whole data set without any filter or the data set filtered with the 2.5 K threshold value. Finally, we consider the results for the three threshold values, to assess the mixed effects of surface heterogeneities and sensor spatial resolutions.

Table 3
Comparison between MODIS and ASTER top of atmosphere (TOA) brightness temperatures over both Africa and Jornada

Scene		MODIS/ASTER bands		
		29/11	31/13	31/14
Africa	RMSD (K)	0.29	0.28	0.42
	bias (K)	− 0.05	− 0.03	0.32
	st. dev. (K)	1.08	1.19	1.14
Jornada	RMSD (K)	0.36	0.48	1.22
	bias (K)	− 0.06	− 0.39	1.20
	st. dev. (K)	1.03	0.99	0.99

St. dev. means the standard deviation of the ASTER aggregated values inside the MODIS pixels for the considered channel.

3. Results and discussion

3.1. Comparing brightness temperature at the sensor level

Fig. 3 and Table 3 display the comparison of the Top of Atmosphere (TOA) or at sensor level estimates of Brightness Temperature (BT), for the three sets of ASTER/MODIS intercompared channels, when considering the coincident nadir observations from both sensors. The agreements were very good for Africa, with RMSD[1] values ranging between 0.28 and 0.42 K. The discrepancy was also low for the Jornada, although larger, with RMSD values ranging between 0.36 and 1.22 K. The better agreement we observed for Africa was ascribed to both (1) lower atmospheric Water Vapor Content (WVC) magnitude and variability (see third paragraph of Section 2.3.2), and (2) lower surface brightness temperatures (see end of Section 2.3.1). Indeed, atmospheric absorption effects increase with both surface temperature and atmospheric WVC when observing hot surfaces (Jacob et al., 2003). The MODIS values were systematically and slightly lower when comparing either bands 29/11 or 31/13, and systematically larger when comparing bands 31/14, with bias[2] values ranging from − 0.38 to 1.19 K. This was consistent with the observations reported when comparing

[1] The Root Mean Square Difference (RMSD) is the mean quadratic difference between two predicted variables.

[2] The bias is the averaged difference between two different estimates.

the waveband averaged atmospheric transmittances over MODIS and ASTER channels (see end of Section 2.1). However, there was no obvious correlation between the magnitudes of these bias values (Table 3) and the differences between the MODIS/ASTER waveband averaged atmospheric transmittances (Table 1). This might be explained by coupling effects between surface emissivity variations, atmospheric perturbations and channel filter response functions. Indeed, the difference between the TOA BT estimates did not depend on atmospheric transmittance only, but also on surface emitted/reflected radiance, which was driven by surface emissivity. Therefore, the spectral variations of both surface emissivity and atmospheric effects induced different waveband brightness temperatures at the sensor level, since the filter response functions of the intercompared MODIS/ASTER channels did not match exactly. The standard deviation of the ASTER aggregated values inside MODIS pixels ranged between 0.99 and 1.24 K (see Table 3). These values resulted from the atmosphere smoothing effect on the spatial variability of the surface outgoing radiance. Finally, the large RMSD value between ASTER band 14 and MODIS band 31 TOA BT for the Jornada was very close to the bias value, whereas the low biases observed in the other cases corresponded to RMSD values ranging between 0.3 and 0.5 K. Therefore, the random differences were lower than 0.5 K, and the systematic differences might be explained by combined effects of surface emissivity variations, atmospheric perturbations, and channel filter response functions. Besides, these

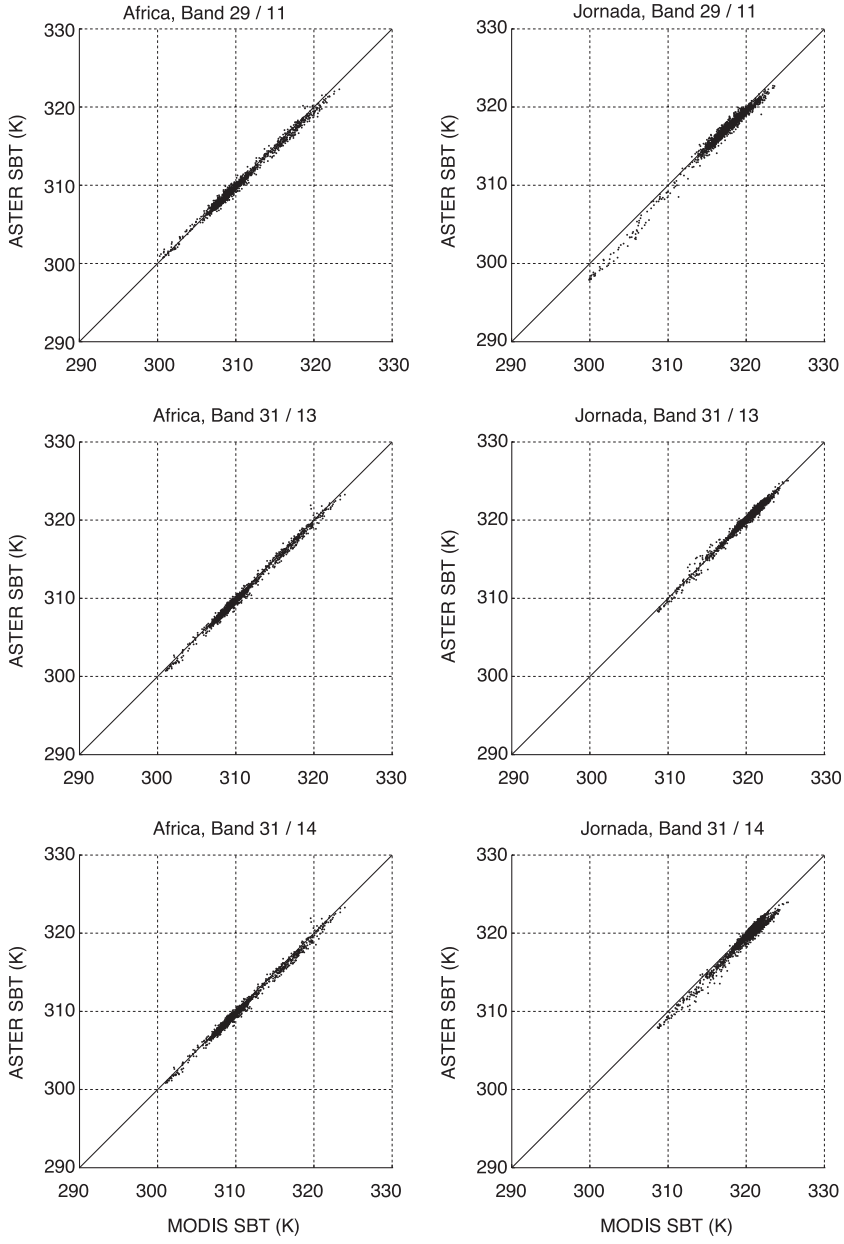

Fig. 4. Scatterplots of MODIS and ASTER Surface Brightness Temperature (SBT) for both the Africa and Jornada scenes. The solid line is the 1:1 line.

differences were close to the estimated accuracies previously mentioned when presenting the MODIS and ASTER products of brightness temperature at the sensor level (Section 2.3.1). This led us to conclude that measurements from both instruments agreed well, which increased the confidence one could have in the instrumental preprocessing, both radiometric and geometric.

3.2. Comparing brightness temperature at the surface level

Fig. 4 displays the scatterplots of MODIS and ASTER estimates of brightness temperature at the surface level, called here Surface Brightness Temperature (SBT), after the atmospheric corrections of the coincident nadir observations. These scatterplots were obtained by considering the MODIS and ASTER data atmospherically processed using the NCEP profiles truncated according to the ground altitude at the profile locations. The first two rows of Table 4 display the statistical results of these scatterplots. Regardless of considered scene and intercompared bands, the MODIS SBT estimates were systematically larger than the ASTER ones. Nevertheless, the differences between MODIS and ASTER retrievals were very low for Africa (RMSD between 0.42 and 0.46 K, bias between 0.18 and 0.32 K), and larger for the Jornada (RMSD between 1.01 and 1.43 K, bias between 0.89 and 1.35 K). The better comparison results we observed for Africa could be explained by the observations reported in the third paragraph of Section 2.3.2. First, we noted for Africa, as compared to the Jornada, a lower difference between the atmospheric WVC value of the NCEP profile used to process the ASTER data and the WVC averaged value over the four surrounding profiles used to process the MODIS data. Second, we noted a lower variability of the WVC values of the four surrounding profiles, which induced a larger similitude between the two different atmospheric correction strategies we chose according to the sensor swaths (see second paragraph of Section 2.3.2). The systematically larger values observed with MODIS for both Africa and Jornada were assumed to result from larger atmospheric corrections applied to the MODIS data. Indeed, the WVC averaged values over the four surrounding NCEP profiles used to process the MODIS images were larger than the WVC values of the single NCEP profiles used to process the ASTER images (see third paragraph of Section 2.3.2). This induced larger MODIS SBT values since the waveband averaged atmospheric transmittances were lower (see Eq. (5)). This assumption was confirmed by performing atmospheric corrections of ASTER data collected over the Jornada with the adjusted NCEP profile, which corresponded to a WVC increase about 0.11 g cm^{-2} as compared to the profile truncated according to the ground altitude at the profile location (see Table 2). The third row of Table 4, labeled "Jornada Adjusted NCEP for ASTER" displays the comparison results for the Jornada when considering the adjusted NCEP profile to atmospherically correct the ASTER data, and the NCEP profiles truncated according to the ground altitude at the profile locations to process the MODIS data. In this case, we observed an increase of the ASTER SBT by 0.2 K regardless of channel (third row of Table 4 as compared to the second). Nevertheless, the MODIS values still were systematically larger as compared to those derived from ASTER. Therefore, we decided to atmospherically correct the ASTER/Jornada data by using a profile having the same WVC as the averaged value over those used to process the MODIS/Jornada data (see Table 2). For this, we increased the humidity of the adjusted NCEP profile by 5% in relative terms. The results are displayed in Table 4 with the label "Jornada Shifted NCEP for ASTER". It is shown that the resulting increase of the ASTER SBT was not the same from one channel to another (fourth row of Table 4 as compared to the third). The remaining differences could result from the spatial variability of the atmospheric variables (atmospheric transmittance, upwelling and downwelling radiances) bilinearly extrapolated from the four surrounding profiles and next used to process MODIS data, as compared to the atmosphere uniformity we assumed when processing the ASTER data. Although the validity of the spatial interpolation method we used was previously shown (Petitcolin & Vermote, 2002), the remaining differences might also result from this bilinear interpolation, as mentioned by Schroedter et al. (2003) who proposed a most robust approach based on the Shepard's method. However, we suspected at this stage that the main reason of these remaining differences for the Jornada was the combined effects of the surface emissivity variations and the filter response functions of the intercompared MODIS/ASTER channels which did not match exactly. Indeed, the Jornada scene included gypsum sand dunes and bare soils of both agricultural and semi-arid areas, which had large spectral variations of emissivity (Schmugge et al., 2002a,b). In

Table 4
Comparison between MODIS and ASTER Surface Brightness Temperatures (SBT) over both Africa and Jornada

Scene		MODIS/ASTER bands		
		29/11	31/13	31/14
Africa	RMSD (K)	0.42	0.43	0.46
	bias (K)	0.19	0.29	0.33
	st. dev. (K)	1.36	1.36	1.32
Jornada	RMSD (K)	1.02	0.72	1.43
	bias (K)	0.89	0.62	1.35
	st. dev. (K)	1.24	1.13	1.15
Jornada Adjusted NCEP for ASTER	RMSD (K)	0.87	0.54	1.22
	bias (K)	0.72	0.41	1.12
	st. dev. (K)	1.25	1.14	1.16
Jornada Shifted NCEP for ASTER	RMSD (K)	0.57	0.15	0.73
	bias (K)	0.41	0.01	0.63
	st. dev. (K)	1.25	1.14	1.17

St. dev. means the standard deviation of brightness temperature of the ASTER aggregated values inside the MODIS pixels for the considered channel. "Jornada Adjusted (respectively Shifted) NCEP for ASTER" means the comparison results when considering the ASTER Jornada scene atmospherically corrected by using the NCEP profile adjusted for surface temperature and humidity conditions (respectively the NCEP profile with a shifted humidity profile).

contrast, the Africa scene included mainly vegetative areas which generally have low spectral variations of emissivity. Finally, the spatial variability of ASTER SBT within MODIS pixels was about 1.3 K. These larger values, compared to the standard deviation of the aggregated values of ASTER TOA BT, were explained by the removal of the atmosphere smoothing effect after atmospheric corrections. We noted that the standard deviation values at 8.5 and 11 μm were similar for Africa, and quite different for the Jornada. This was explained by the spatial variability of emissivity at 8.5 μm inside the ASTER Jornada scene, and was consistent with the results reported by Schmugge et al. (2002b). For further investigations with the Jornada data, we selected the ASTER SBT estimates which were the closest to the MODIS ones, i.e. those computed using the shifted NCEP profile.

3.3. Comparing surface emissivity and radiometric temperature

Fig. 5 and Table 5 display the comparison of MODIS and ASTER emissivity estimates. MODIS retrievals were obtained by applying the calculated TIR emissivities to the surface brightness temperature images, where the TIR emissivities were derived both characterizing the MIR

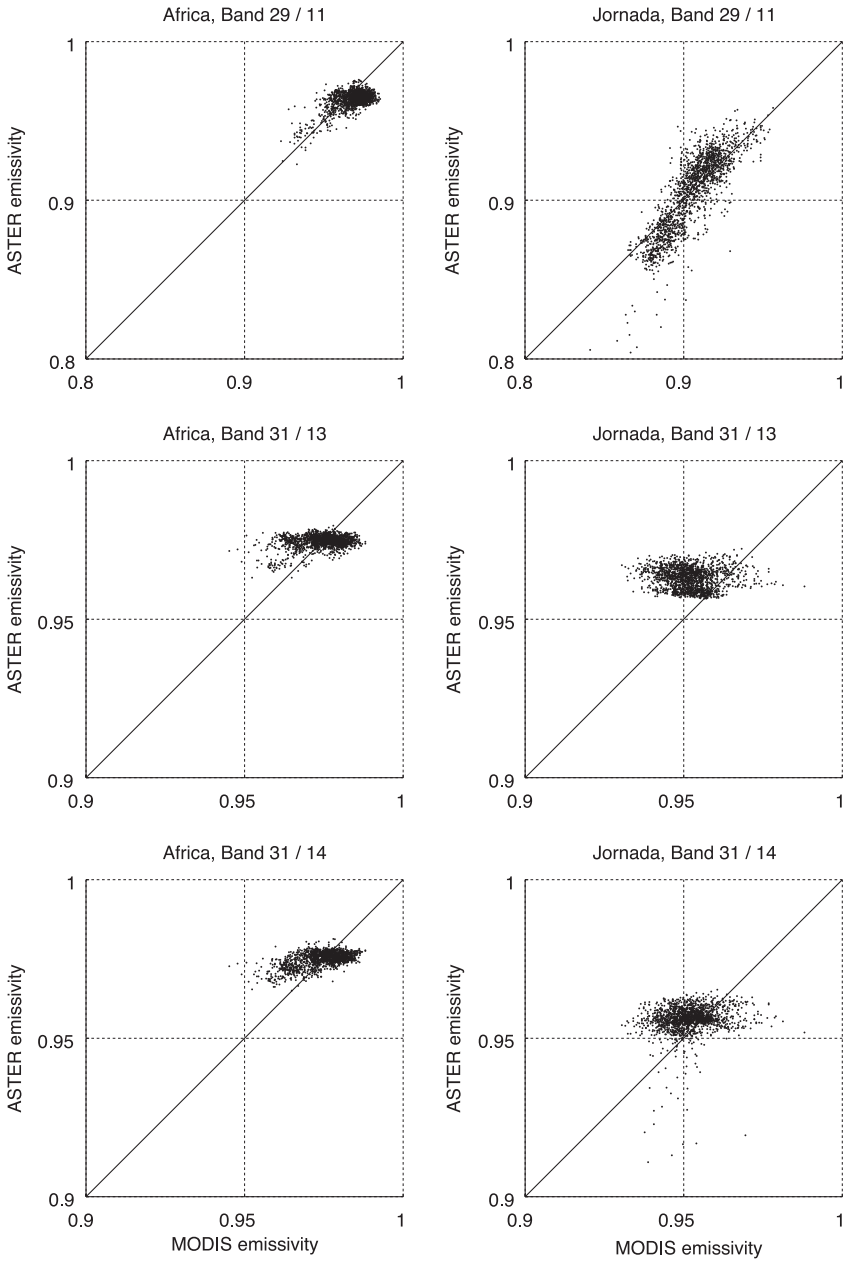

Fig. 5. Scatterplots of MODIS and ASTER surface emissivity estimates for both the Africa and Jornada scenes. The solid line is the 1:1 line. For a better display, the axis range between 0.8 and 1, and 0.9 and 1, when considering the ASTER/MODIS bands 29/11, and bands 31/13 and 31/14, respectively.

Table 5
Comparison between MODIS and ASTER emissivity estimates over both Africa and Jornada

Scene		MODIS/ASTER bands		
		29/11	31/13	31/14
Africa	RMSD	0.009	0.006	0.006
	bias	0.005	0.0001	− 0.0004
	st. dev.	0.009	0.004	0.004
Jornada	RMSD	0.016	0.014	0.008
	bias	0.002	− 0.011	− 0.004
	st. dev.	0.012	0.002	0.003

St. dev. means the standard deviation of emissivity of the ASTER aggregated values inside the MODIS pixels for the considered channel.

BRDF and computing TISIE over a 16-day period. ASTER retrievals were derived from the five surface brightness temperature images. Consequently, the time meanings of ASTER and MODIS estimates were significantly different. This induced difficulties to link the comparison results for emissivity or radiometric temperature to those obtained when dealing with SBT. For Africa, the ranges of emissivity estimates from both sensors were quite narrow, i.e. between 0.93 and 0.97, regardless of intercompared channels. This was explained by the study area which was a Savannah landscape, and therefore a vegetative area with low spectral variations of emissivity. The statistical indicators showed that the estimates from both sensors agreed very well (RMSD and bias values ranging from 0.006 to 0.009, and from − 0.0004 to 0.005, respectively). For the Jornada, the ranges of emissivity estimates from both sensors at 8.6 μm were broader as compared to those observed for Africa, i.e. between 0.84 and 0.96. These larger ranges were explained by the extensive gypsum sand dunes and the Jornada semi-arid rangeland, which both had low values of emissivity at 8.6 μm (Schmugge et al., in press). In contrast, the ranges at 11 μm were similar to those observed for Africa. This was explained by the emissivity variations for natural surfaces which are generally low around this wavelength. The comparison results were not as good as those observed for Africa, but they were acceptable (RMSD and bias values ranging from 0.008 to 0.016, and from − 0.01 to 0.002, respectively). For both study areas, the ranges of MODIS and ASTER values at 8.6 μm were very similar, whereas the range of MODIS emissivity at 11 μm was larger as compared to that of ASTER estimates (see Fig. 5). For the latter wavelength, the scatterplots indicated low correlations between MODIS and ASTER retrievals. We might in this case have reached the limitations of both algorithms. At the high end, the lower ASTER values could be due to the gray body problem of TES, when MMD values become very low. As a result, ASTER did not observe the higher emissivities for vegetated fields. For the low end, the MODIS results were not consistent with the laboratory emissivity spectra derived from samples collected over the Jornada. Indeed, these spectra did not yield many values around and below 0.95 at 11 μm (Schmugge et al., 2002b). However, the lower MODIS values could result from the large scale of the MODIS data, as noted by Becker and Li (1995) when dealing with coarser spatial resolutions. The values of the standard deviation of the ASTER emissivities inside MODIS pixels varied significantly from one channel to another for both study areas, and were systematically larger at 8.6 μm. This was explained by the emissivity variability which is generally larger at this wavelength than at 11 μm.

Fig. 6 and Table 6 display the comparison of the MODIS and ASTER retrieved Surface Radiometric Temperatures

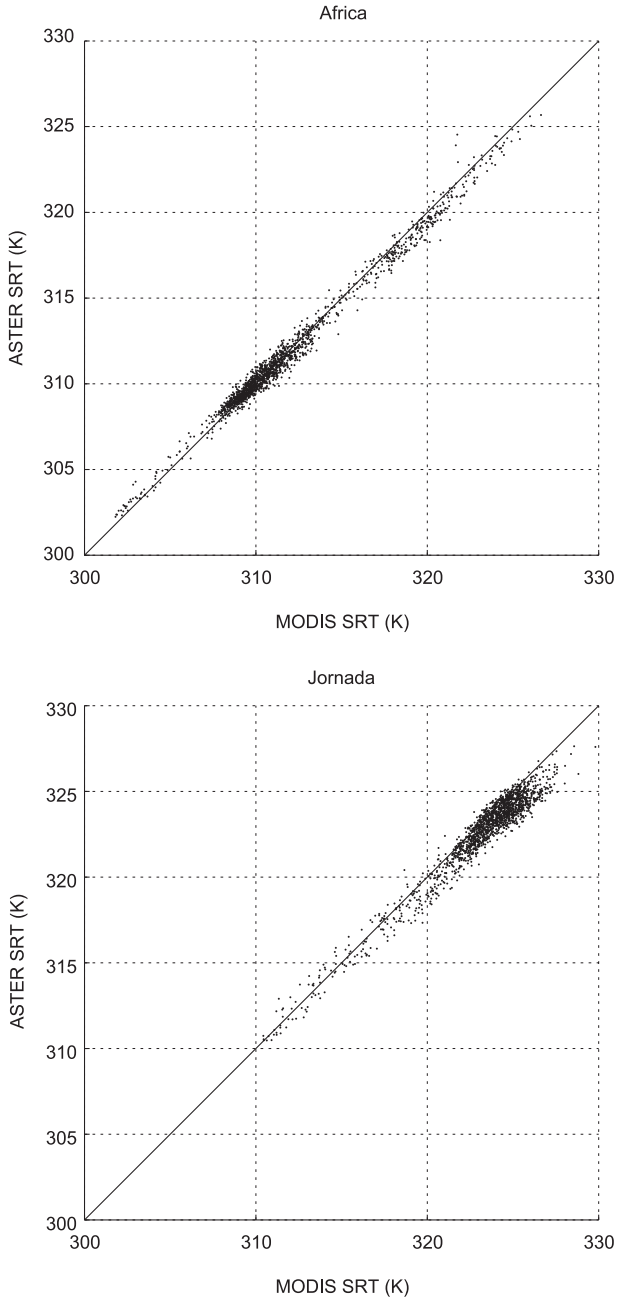

Fig. 6. Scatterplots of MODIS and ASTER Surface Radiometric Temperatures (SRT) estimates for both the Africa and Jornada scenes. The solid line is the 1:1 line.

Table 6
Comparison between MODIS and ASTER Surface Radiometric Temperatures (SRT) estimates over both Africa and Jornada

Scene		SRT
Africa	RMSD (K)	0.50
	bias (K)	0.06
	st. dev. (K)	1.41
Jornada	RMSD (K)	0.86
	bias (K)	0.67
	st. dev. (K)	1.19

St. dev. means the standard deviation of radiometric temperature of the ASTER aggregated values inside the MODIS pixels.

(SRT). For Africa, the estimates were very close, with a low RMSD value and a negligible bias value (0.5 and 0.06 K, respectively). Besides, the RMSD value was very close to those observed for SBT. For the Jornada, the MODIS values were larger than those from ASTER. The discrepancy was ascribed to the differences between the intrinsic features of the algorithms regarding surface properties, whereas no explanation was found for the remaining bias. Overall, the RMSD values, i.e. 0.5 K for Africa and 0.86 K for the Jornada, were lower than the algorithm accuracies estimated by previous studies (see third paragraph of Introduction). This indicated the consistency between the algorithms, despite their relying on different assumptions and underlying physics (see first paragraph of Section 2.2). The standard deviation of the ASTER SRT values inside the MODIS pixels was 0.3 K larger for Africa than for the Jornada. This was explained by the pattern the scenes displayed. At the larger scale (i.e. the scale of the scenes), the Africa scenes included one kind of pattern, i.e. Savannah landscape, whereas the Jornada scenes included different kinds of surface (i.e. mountainous areas, gypsum sand dune, agricultural fields and semi-arid rangelands). At the lower scale, i.e. kilometer scale, however, the Jornada scenes displayed a lower spatial variability since a given type of land use was more homogeneous than Savannah bushes.

The differences between ASTER and MODIS emissivities/SRT could be explained by the assumptions the algorithms relied on, and their resulting limitations. Petitcolin and Vermote (2002) observed a low signal to noise ratio when fitting the Li-Ross BRDF kernel driven model over the MODIS retrieved MIR reflectances, which could induce significant errors when estimating the MIR and then the TIR emissivities. Moreover, the multidirectional MIR reflectance data sets provided directional samplings in a plane that is $\sim 35^\circ$ from the principal plane, whereas Weiss et al. (2002) showed that the performances of BRDF kernel-driven models can be poor outside the principal plan. Besides, the algorithm assumes that both TISIE and MIR BRDF do not change dramatically over 16-day periods. As explained in Section 2.2.2, the TES algorithm relies on a semi-empirical relationship between the minimum value and the contrast of emissivity, which was previously calibrated using emissivity spectra measured in laboratory from samples collected around the world (Schmugge et al., 1998a). However, there were probably significant differences between the laboratory measurements and the larger scale of the ASTER data. Indeed, the laboratory samples used for the calibration of the TES empirical relationship were homogeneous whereas the algorithm was applied on ASTER 90 m spatial resolution pixels which depicted spatial heterogeneities. Nevertheless, we were more confident in the ASTER retrievals for the Jornada, since they agreed well with ground-based measurements, especially over the relatively homogeneous White Sands gypsum dunes (Schmugge et al., 2002b). A better understanding of the good comparison results for radiometric temperature despite differences in emissivity retrievals at 11 μm would require deeper investigations on both algorithms, which was out of the scope of this study. We note that we observed significant differences (up to 2 K) between algorithm SRT retrievals when considering ASTER SBT computed using the raw NCEP profile rather than the shifted one. This emphasized the strong influence of the atmospheric performances on those of the TES algorithm, as previously observed by Schmugge et al. (1998a).

3.4. Assessing the combined effects of surface heterogeneity and spatial resolution

Finally, we assessed the combined effects of spatial resolution and heterogeneity by comparing the MODIS and ASTER radiometric temperature estimates for different levels of variability of the ASTER radiometric temperature retrievals. As previously explained (end of Section 2.3.3), the level of variability was characterized using threshold values of the standard deviation of the ASTER radiometric temperatures aggregated inside MODIS pixels. The comparison of the algorithm retrievals for the different threshold values is displayed in Table 7. The lower the threshold

Table 7
Comparison between MODIS and ASTER radiometric temperatures for different level of variability of the ASTER aggregated values inside MODIS pixels

Filter threshold value (K)		Africa	Jornada
2.5	pix. numb.	1661	1662
	RMSD (K)	0.50	0.92
	bias (K)	0.06	0.64
	st. dev. (K)	1.41	1.16
1	pix. numb.	548	887
	RMSD (K)	0.37	0.86
	bias (K)	− 0.04	0.60
	st. dev. (K)	0.75	0.77
0.5	pix. numb.	38	46
	RMSD (K)	0.34	0.66
	bias (K)	− 0.11	0.21
	st. dev. (K)	0.44	0.44

St. dev. means the standard deviation of radiometric temperature of the ASTER aggregated values. Pix. numb means the number of selected pixels for the comparison, after the removal of the ASTER aggregated values that corresponded to a st. dev. larger than the threshold value.

value, the better were the comparison results. This indicated that both algorithms agreed better when the spatial variability was lower. However, the difference between the maximum and minimum RMSD values of radiometric temperature when considering the three threshold values was 0.16 and 0.26 K for Africa and Jornada, respectively. This showed that the spatial variability was not a critical issue for the scenes we considered. It was consistent with the comparison results we obtained when running the TES algorithm over the ASTER scenes degraded to the MODIS spatial resolution, since we did not observed significantly different results. These observations led us to conclude that the MODIS/TISIE and ASTER/TES algorithms were robust regarding the spatial variability within these study areas.

4. Conclusion

The scope of this study was to compare estimates of surface emissivity and radiometric temperature derived from measurements collected using the MODIS and ASTER sensors. Two areas were selected to conduct the comparison. The first area, called the Jornada, was located in northern Chihuahuan desert, New Mexico, USA, and included semi-arid rangelands, agricultural areas, mountainous areas and gypsum sand dunes. The second area was a Savannah landscape located in the Central African Republic, central Africa. The MODIS and ASTER estimates were retrieved using the TISIE algorithm proposed by Petitcolin and Vermote (2002), and the TES algorithm proposed by Schmugge et al. (1998a, 2002a), respectively. Such investigations were of interest since the algorithms relied on different assumptions according to the temporal, spectral and directional information provided by each sensor. The comparison between MODIS/TISIE and ASTER/TES retrievals was possible since ASTER and MODIS are on board the same platform, which eliminated temporal problems due to the nonstable nature of kinetic temperature. For a better understanding of the results we obtained when comparing surface radiometric temperatures and emissivities, we first intercompared the intermediate variables, i.e. brightness temperatures at the sensor and surface levels. Intercomparisons of brightness temperatures and emissivities were performed for ASTER/MODIS matching bands at 8.6 and 11 μm.

Both TES and TISIE algorithms required performing atmospheric corrections to estimate surface outgoing and atmospheric downwelling radiances. These corrections were performed using the MODTRAN 4 radiative transfer code along with NCEP profiles. We used the same profiles for both sensors when characterizing atmosphere state. However, the instrument swaths led us to use different strategies when considering the spatial variability of the atmosphere radiative properties. The comparison of the MODIS and ASTER brightness temperatures at the sensor level showed that the discrepancy (0.5 K) was close to the estimated accuracies of both sensors, whereas the systematic errors could be explained by the combination of surface, atmospheric and instrumental effects. The comparison of the brightness temperatures at the surface level showed a very good agreement for Africa. For the Jornada, we had to reconsider the atmospheric corrections of the ASTER data to obtain estimates close to those derived from MODIS. Then, the remaining differences (ranging from 0.4 to 0.7 K) were ascribed to the combined effects of surface emissivity variations and channel filter response functions. These investigations showed that using the same atmospheric profiles when characterizing atmospheric state may not be sufficient to perform accurate atmospheric corrections. Indeed, these require accounting for the atmospheric spatial variability when the level of the latter is large.

When comparing emissivity estimates, we observed very good agreements for Africa. The agreement for the Jornada was also good despite larger discrepancies as compared to Africa. Overall, the differences ranged between 0.006 and 0.016. The broad range of emissivity at 8.6 μm for the Jornada was well displayed by both sensors. However, we observed a larger range of MODIS emissivity values compared to that of ASTER retrievals at 11 μm for both study areas. The larger MODIS values were ascribed to the gray body problem of the TES algorithm, whereas the lower MODIS values were not consistent with the emissivity laboratory spectra derived from samples collected over the Jornada. When comparing surface radiometric temperature estimates, once more, the results were excellent for Africa and good for the Jornada. Overall, the remaining differences (0.9 K) were lower than the TES/TISIE accuracies reported by previous studies, and corresponded to the requirement for many applications. Since the applied atmospheric corrections were performed such as surface brightness temperature estimates from both sensors were very close, these remaining differences could results from the experimental context, the differences in time meaning of ASTER and MODIS retrievals, and the different underlaying physics of both algorithms. Finally, we assessed a possible impact of the combination of the sensor spatial resolutions and the spatial variability displayed by the observed natural surfaces. It was shown that these combined effects were not critical for the study areas we considered.

The low differences in surface radiometric temperature we observed indicated the agreement between the algorithms and their consistencies. However, it was not possible to draw a general conclusion that would require a larger database and therefore much attention on the performances of the atmospheric corrections at the global scale. It was shown that the combined effects of sensor spatial resolution and spatial variability were not critical for the study areas we considered. Therefore, ASTER and MODIS TIR products should be used in the framework of the JORNEX campaign for future investigations focused on spatial and temporal issues in remote sensing. First, aggregation processes that occur when modeling surface energy fluxes at

the MODIS scale may be studied using ASTER high spatial resolution data. Second, the complementarity between both sensor revisits, i.e. 16 days for ASTER and everyday for MODIS, will be of interest to assess strategies of data assimilation in modeling approaches which dynamically describe energetic exchanges at the surface–atmosphere interface (Olioso et al., 2002). Finally, extending ASTER results over a limited area to the global scale provided by MODIS is a promising issue (Zhou et al., 2003). Merging ASTER and MODIS emissivity data may further results in worldwide emissivity maps which take advantage of both sensors in terms of spatial and temporal sampling and coverage.

Acknowledgements

This study was supported by the ASTER and MODIS Projects of NASA's EOS-TERRA Program. The authors wish to thank reviewers for valuable comments.

References

Barducci, A., & Pippi, Y. (1996). Temperature and emissivity retrieval from remotely sensed images using the "Grey Body Emissivity" method. *IEEE Transactions on Geoscience and Remote Sensing*, *34*, 681–695.

Barnes, W., Pagano, T., & Salomonson, V. (1998). Prelaunch characteristics of the Moderate Resolution Imaging Spectroradiometer (MODIS) on EOS-AM1. *IEEE Transactions on Geoscience and Remote Sensing*, *36*, 1088–1100.

Becker, F. (1987). The impact of spectral emissivity on the measurement of land surface temperature from a satellite. *International Journal of Remote Sensing*, *8*, 1509–1522.

Becker, F., & Li, Z. (1990). Temperature Independent Spectral Indices in thermal infrared bands. *Remote Sensing of Environment*, *32*, 17–33.

Becker, F., & Li, Z. (1995). Surface temperature and emissivity at various scale: Definition, measurement and related problem. *Remote Sensing Reviews*, *12*, 225–253.

Berk, A., Bernstein, L., Anderson, G., Acharya, P., Robertson, D., Chetwynd, J., & Adler-Golden, S. (1998). MODTRAN cloud and multiple scattering upgrades with application to AVIRIS. *Remote Sensing of Environment*, *65*, 367–375.

Caselles, V., Valor, E., Coll, C., & Rubio, E. (1997). Thermal band selection for the PRISM instrument: Part 1. Analysis of emissivity–temperature separation algorithms. *Journal of Geophysical Research*, *102*, 11145–11164.

Coll, C., Caselles, V., Rubio, E., Sospedra, F., & Valor, E. (2000). Temperature and emissivity separation from calibrated data of the Digital Airborne Imaging Spectrometer. *Remote Sensing of Environment*, *76*, 250–259.

Dash, P., Göttsche, F. -M., Olesen, F. -S., & Fischer, H. (2002). Land surface temperature and emissivity estimation from passive sensor data: theory and practice-current trends. *International Journal of Remote Sensing*, *23*(13), 2563–2594.

Derber, J., Parrish, D., & Lord, S. (1991). The new global operational analysis system at the National Meteorological Center (NMC). *Weather and Forecasting*, *6*, 538–547.

Derber, J., & Wu, W. (1998). The use of TOVS cloud-cleared radiances in the NCEP SSI analysis system. *Monthly Weather Review*, *126*, 2287–2299.

Fujisada, H. (1998). ASTER Level-1 data processing algorithm. *IEEE Transactions on Geoscience and Remote Sensing*, *36*, 1101–1112.

Fujisada, H., Sakuma, F., Ono, A., & Kudoh, M. (1998). Designed and preflight performances of ASTER Instrument protoflight model. *IEEE Transactions on Geoscience and Remote Sensing*, *36*, 1152–1160.

Gillespie, A. (1985). Lithologic mapping of silicate rocks using TIMS. *The TIMS data user workshop, June 18–19, 1985.* JPL Publication 86–38, pp. 29–44.

Gillespie, A., Rokugawa, S., Hook, S., Matsunaga, T., & Kahle, A. (1996). Temperature/emissivity separation algorithm. Theoretical basis document, version 2.1. Greenbelt, MD, USA: NASA/GSFC.

Gillespie, A., Rokugawa, S., Matsunaga, T., Cothern, S., Hook, S., & Kahle, A. (1998). A temperature and emissivity separation algorithm for Advanced Spaceborne Thermal Emission and Reflection radiometer (ASTER) images. *IEEE Transactions on Geoscience and Remote Sensing*, *36*, 1113–1126.

Havstad, K., Kustas, W., Rango, A., Ritchie, J., & Schmugge, T. (2000). Jornada experimental range: a unique arid land location for experiments to validate satellite system. *Remote Sensing of Environment*, *53*, 13–25.

Jacob, F., Gu, X., Hanocq, J. -F., & Baret, F. (2003). Atmospheric corrections of single broadband channel and multidirectional airborne thermal infrared data. Application to the ReSeDA Experiment. *International Journal of Remote Sensing*, *24*, 3269–3290.

Jacob, F., Olioso, A., Gu, X., Su, Z., & Seguin, B. (2002). Mapping surface fluxes using visible, near infrared, thermal infrared remote sensing data with a spatialized surface energy balance model. *Agronomie: Agriculture and Environment*, *22*, 669–680.

Justice, C., Vermote, E., Townshend, J., Defries, R., Roy, D., Hall, D., Salomonson, V., Privette, J., Riggs, G., Strahler, A., Lucht, W., Myneni, R., Knyazikhin, Y., Running, S., Nemani, R., Wan, Z., Huete, A., van Leeuwen, W., Wolfe, R., Giglio, L., Muller, J. -P., Lewis, P., & Barnsley, M. (1998). The MODerate Imaging Spectroradiometer (MODIS): land remote sensing for global change research. *IEEE Transactions on Geoscience and Remote Sensing*, *36*, 1228–1249.

Li, Z. -L., & Becker, F. (1993). Feasibility of land surface temperature and emissivity determination from AVHRR data. *Remote Sensing of Environment*, *43*, 67–85.

Li, Z. -L., Becker, F., Stoll, M., & Wan, Z. (1999). Evaluation of six methods for extracting relative emissivity spectra from thermal infrared images. *Remote Sensing of Environment*, *69*, 197–214.

Matsunaga, T. (1994). A temperature–emissivity separation method using an empirical relationship between the mean, the maximum and the minimum of the thermal infrared emissivity spectrum. *Journal of the Remote Sensing Society of Japan*, *14*, 230–241.

Nerry, F., Peticolin, F., & Stoll, M. (1998). Bidirectional reflectivity in AVHRR Channel 3: Application to a region in Northern Africa. *Remote Sensing of Environment*, *66*, 298–316.

Norman, J., & Becker, F. (1995). Terminology in thermal infrared remote sensing of natural surfaces. *Remote Sensing Reviews*, *12*, 159–173.

Ogawa, K., Schmugge, T., Jacob, F., & French, A. (2002). Estimation of broadband land surface emissivity from multispectral thermal infrared remote sensing. *Agronomie: Agriculture and Environment*, *22*, 695–696.

Ogawa, K., Schmugge, T., Jacob, F., & French, A. (2003). Estimation of land surface window (8–12μm) emissivity from multi-spectral thermal infrared remote sensing—A case study in a part of Sahara Desert. *Geophysical Research Letters*, *30*, 1067–1071.

Olioso, A., Braud, I., Chanzy, A., Courault, D., Demarty, J., Kergoat, L., Lewan, L., Ottlé, C., Prévot, L., Zhao, W., Calvet, J., Cayrol, P., Jongschaap, R., Moulin, S., Noilhan, J., & Wigneron, J. -P. (2002). SVAT modeling over the Alpilles-ReSeDA experiment: Comparison of SVAT models, first results on wheat. *Agronomie: Agriculture and Environment*, *22*, 651–668.

Olioso, A., Chauki, H., Courault, D., & Wigneron, J. (1999). Estimation of evapotranspiration and photo-synthesis by assimilation of remote sensing data into SVAT models. *Remote Sensing of Environment*, *68*, 341–356.

Petitcolin, F., Nerry, F., & Stoll, M. -P. (2002a). Mapping directional emissivity at 3.7 using a simple model of bi-directional reflectivity. *International Journal of Remote Sensing*, *23*, 3443–3472.

Petitcolin, F., Nerry, F., & Stoll, M. -P. (2002b). Mapping temperature

independent spectral indice of emissivity and directional emissivity in avhrr channels 4 and 5. *International Journal of Remote Sensing*, *23*, 3473–3491.

Petitcolin, F., & Vermote, E. (2002). Land surface reflectance, emissivity and temperature from MODIS middle and thermal infrared data. *Remote Sensing of Environment*, *83*, 112–134.

Schmugge, T., French, A., Ritchie, J., Rango, A., & Pelgrum, H. (2002a). Temperature and emissivity separation from multispectral thermal infrared observations. *Remote Sensing of Environment*, *79*, 189–198.

Schmugge, T., Hook, S., & Coll, C. (1998a). Recovering surface temperature and emissivity from thermal infrared multispectral data. *Remote Sensing of Environment*, *65*, 121–131.

Schmugge, T., Jacob, F., French, A., Ritchie, J., Chopping, M., & Rango, A. (2002b). ASTER thermal infrared observations over New Mexico. *IGARSS'2002 (Totonto, Canada), International Geoscience and Remote Sensing Symposium*, *vol. 1* (pp. 24–26). Piscataway, NJ: IEEE.

Schmugge, T., & Kustas, W. (1999). Radiometry at infrared wavelengths for agricultural applications. *Agronomie: Agriculture and Environment*, *19*, 83–96.

Schmugge, T., Kustas, W., & Humes, K. (1998b). Monitoring land surface fluxes using ASTER observations. *IEEE Transactions on Geoscience and Remote Sensing*, *36*, 1421–1430.

Schroedter, M., Olesen, F. -S., & Fischer, H. (2003). Determination of land surface temperature distributions from single channel IR measurements: an effective spatial interpolation method for the use of TOVS, ECMWF, and radiosonde profiles in the atmospheric correction scheme. *International Journal of Remote Sensing*, *24*, 1189–1196.

Seguin, B., Becker, F., Phulpin, T., Gu, X., Guyot, G., Kerr, Y., King, C., Lagouarde, J., Ottlé, C., Stoll, M., Tabbagh, T., Vidal, A. (1999). IRSUTE: A minisatellite project for land surface heat flux estimation from field to regional scale. *Remote Sensing of Environment*, *68*, 357–369.

Snyder, W., Wan, Z., Zhang, Y., & Feng, Y. -Z. (1998). Classification-based emissivity for land surface temperature measurement from space. *International Journal of Remote Sensing*, *19*, 2753–2774.

Sobrino, J., & Raissouni, N. (2000). Toward remote sensing methods for land cover dynamic monitoring. Application to Morroco. *International Journal of Remote Sensing*, *21*, 353–366.

Sobrino, J., Raissouni, N., & Li, Z. (2000). A comparative study of land surface emissivity retrieval from NOAA data. *Remote Sensing of Environment*, *75*, 256–266.

Valor, E., & Caselles, V. (1996). Mapping land surface emissivity from NDVI: Application to European, African and South American areas. *Remote Sensing of Environment*, *57*, 167–184.

Wan, Z., & Dozier, J. (1996). A generalized split-window algorithm for retrieving land-surface temperature from space. *IEEE Transactions on Geoscience and Remote Sensing*, *34*, 892–905.

Wan, Z., & Li, Z. -L. (1997). A physics-based algorithm for retrieving land-surface emissivity and temperature from EOS/MODIS data. *IEEE Transactions on Geoscience and Remote Sensing*, *35*, 980–996.

Wanner, W., Li, X., & Strahler, A. (1995). On the derivation of kernels for kernel-driven models of bidirectional reflectance. *Journal of Geophysical Research*, *100*, 21077–21089.

Watson, K. (1992). Two-temperature method for measuring emissivity. *Remote Sensing of Environment*, *42*, 117–121.

Weiss, M., Jacob, F., Baret, F., Pragnére, A., Bruchou, C., Leroy, M., Hautecoeur, O., Prvot, L., & Bruguier, N. (2002). Evaluation of kernel-driven BRDF models for the normalization of Alpilles/ReSeDA PolDER data. *Agronomie: Agriculture and Environment*, *22*, 531–536.

Xiong, X., Chiang, K., Guenther, B., & Barnes, W. (2003). MODIS thermal emissive bands calibration algorithm and on-orbit performance. In H. -L. Huang, D. Lu, & Y. Sasano (Eds.), *Proceedings of SPIE—Optical remote sensing of the atmosphere and clouds III, vol. 4891* (pp. 392–401).

Yamaguchi, Y., Kahle, A., Tsu, H., Kawakami, T., & Pniel, M. (1998). Overview of Advanced Space-borne Thermal Emission and Reflection Radiometer (ASTER). *IEEE Transactions on Geoscience and Remote Sensing*, *36*, 1282–1289.

Zhou, L., Dickinson, R., Ogawa, K., Tian, Y., Jin, M., & Schmugge, T. (2003). Relations between albedos and emissivities from MODIS and ASTER data over North African Desert. *Geophysical Research Letters*, *30*, 2026–2029.